ACS APPLIED NANO MATERIALS

www.acsanm.org Article

# Achieving High-Sensitivity Wide-Range Strain Sensing with 0D-2D MXene/Ag NPs Composite Structures

Jintao Zhang,[§] Yina Yang,[§] Ranran Wang, Jing Sun, Liangjing Shi, Yin Cheng,* and Yucai Shen*

Cite This: *ACS Appl. Nano Mater.* 2025, 8, 10022−10032 Read Online

ACCESS | Metrics & More | Article Recommendations | Supporting Information

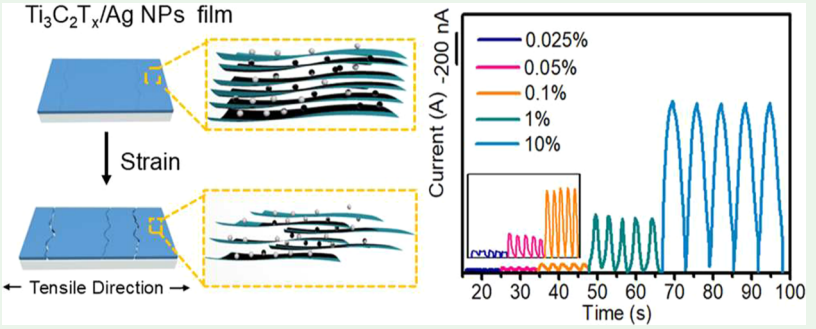


**ABSTRACT:** Stretchable and wearable strain sensors hold significant potential in human motion monitoring and health management, yet the mutual constraints between sensitivity and stretchability remain a critical challenge. This study proposes a multidimensional composite network structure based on MXene and silver nanoparticles (Ag NPs) to address the limited strain range caused by the close interlayer stacking and strong interaction forces in two-dimensional materials. By embedding Ag NPs into the interlayers of MXene, the interlayer spacing was significantly expanded, which weakened interlayer forces and facilitated effective slippage, thereby synergistically enhancing the sensor performance. Experimental results demonstrated that with 5 wt % Ag NPs doping, the sensor exhibited exceptional comprehensive performance: a sensitivity (gauge factor, GF) exceeding 153.28 across a strain range of 0−51.5%, a maximum detectable strain of 51.5%, a low detection limit of 0.025%, and robust cyclic stability over 5000 stretching cycles. Mechanistic studies revealed that Ag NPs suppressed crack propagation through a lubricating effect while increasing conductive contact points to enhance sensitivity. Furthermore, the sensor achieved real-time monitoring of human physiological signals (e.g., pulse, swallowing, and joint movements), highlighting its potential for wearable health monitoring. This work provides novel insights into optimizing the performance of two-dimensional materials in flexible electronic devices.

**KEYWORDS:** *strain sensor, wearable electronics, MXene, Ag NPs*



## INTRODUCTION

Stretchable and wearable strain sensors[1−5] have attracted considerable research efforts recently due to their promising applications in motion monitoring,[6−8] disease diagnosis, personal health care,[9,10] intelligent human/machine interactions,[11−13] and so forth. However, sensitivity and stretchability, which are the two most critical performance indicators, are mutually constrained due to their opposite requirements on the sensing material structure.[14] In detail, achieving high sensitivity requires the strain sensor to undergo a large change in the conductive network structure under very small strains, while achieving high stretchability requires the sensor to maintain good conductive pathways within a large strain range. The two pin down each other, and growth on one side leads to sacrifice on the other.[15,16] Therefore, to develop strain sensors with both high sensitivity and broad strain sensing range is a grand challenge, and to realize a performance index that the sensitivity (gauge factor (GF)) is over 100 with the entire strain range and the maximum strain sensing range reaches 50% is essential for satisfying the detection of full-range human body motions, which further increases the pressure to enhance the sensing performance.[17−19]

Currently, complicated microstructures of substrates and sensing materials have been designed to balance the two performances. The former, for example, introducing microstructures such as bionic structures,[20] grids on the flexible substrates by means of transfer, photolithography, etc.,[21,22] or introducing wrinkles, cracks, etc. on the substrate by means of prestretching, etc.[23−26] However, these methods usually require high precision of the manufacturing process and high

Received: March 9, 2025
Revised: April 21, 2025
Accepted: April 25, 2025
Published: May 7, 2025

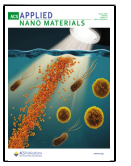




https://doi.org/10.1021/acsanm.5c01438
*ACS Appl. Nano Mater.* 2025, 8, 10022−10032

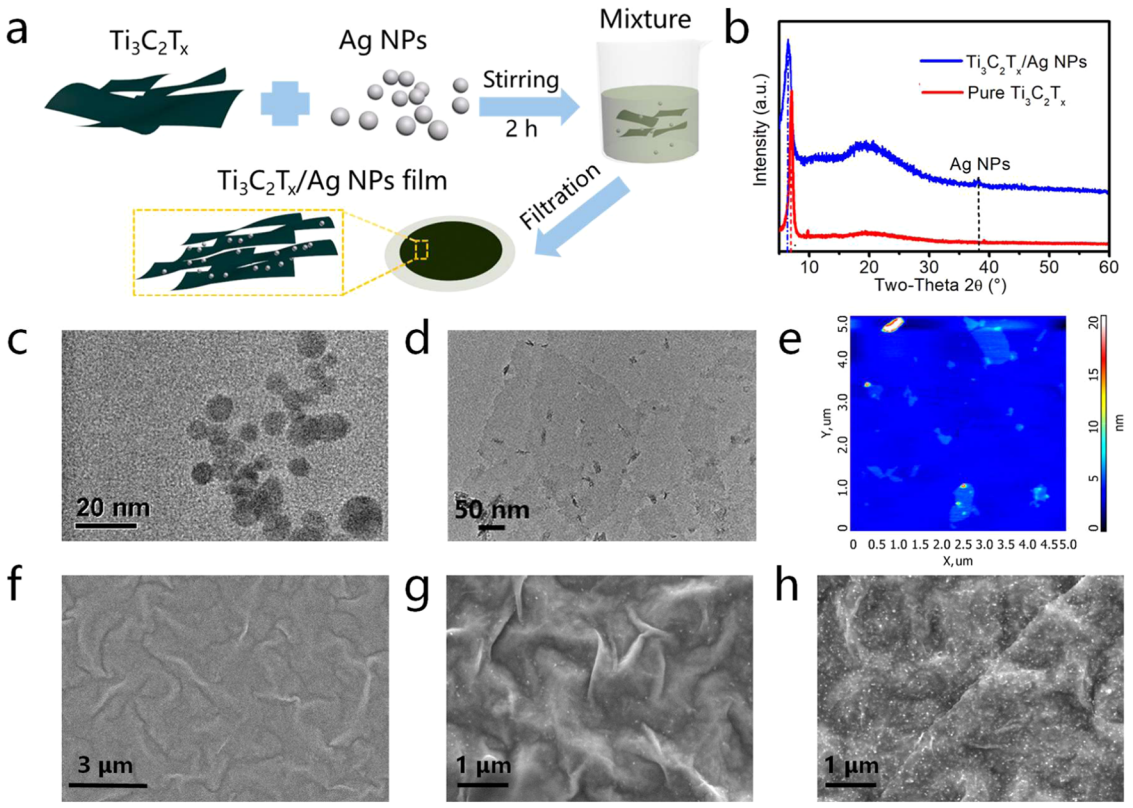


**Figure 1.** (a) Fabrication process of the $Ti_3C_2T_x$/Ag NPs composite film. (b) XRD pattern of $Ti_3C_2T_x$ and $Ti_3C_2T_x$/Ag NPs films. TEM images of (c) Ag NPs and (d) $Ti_3C_2T_x$. (e) AFM images of $Ti_3C_2T_x$ sheets. Top-view SEM images of the (f) $Ti_3C_2T_x$ film, (g) $Ti_3C_2T_x/Ag_5$ film, and (h) $Ti_3C_2T_x/Ag_{30}$ film.

consumption of time, which hinder their applications in large-scale manufacturing. The design of special sensitive material microstructures is a more economical and practical way, and due to the richness of material variety, the types of microstructures that are constructed will have more possibilities, such as sandwich structure, layered structure, nacre-like structure, etc.[17,18,27] Among them, the composition of multidimensional materials is a very common method because materials of different dimensions have distinct merits and boundness as the sensitive materials of strain sensors. For instance, zero-dimensional materials such as carbon black and metal nanoparticles are relatively short in length, and the conductive sensitive elements are easily separated during the stretching process, which impedes the sensor from obtaining a wide range of strain sensing.[28,29] While one-dimensional materials such as carbon nanotubes and metal nanowires generally have high aspect ratios, during the stretching process, the nanowires or nanoribbons are easily entangled with each other to maintain the conductive pathways, and the conductive network structure changes little. So, although the strain sensor usually has a wide strain sensing range, its sensitivity will be very low.[30] In contrast, two-dimensional materials such as graphene cannot be effectively slipped during the stretching process due to the close stacking of the sheets and the existence of van der Waals forces, hydrogen bonding, and other interaction forces, which facilitate the generation and propagation of large cracks that block the conductive pathways, normally leading to an ultrahigh sensitivity but a very narrow strain sensing range of strain sensors.[31−34] Therefore, taking advantage of the structural characteristics of materials of different dimensions to bring their superiority into full play and compensate for their respective shortcomings is a very effective way to improve the comprehensive performance of the strain sensor.

MXenes, which represent a new kind of early transition metal carbide or carbonitride, are a new type of graphene-like two-dimensional layered crystalline materials. The unified chemical formula of MXenes is Mn+1XnTx, where n = 1, 2, 3, M stands for transition metal elements (can be one or more elements), X represents carbon or/and nitrogen element, T means a surface terminations (such as −OH, −O and −F), and x is the number of surface terminations.[35,36] Because of their good electrical conductivity, hydrophilicity, stability, mechanical properties, etc., MXenes have been widely applied in various areas, including energy storage, catalysis, and photothermal therapy.[37−41] Especially their excellent conductivity and flexibility make them one kind of ideal conductive sensitive materials suitable for flexible strain sensors. However, as two-dimensional materials, MXenes also have the common problem of two-dimensional sensitive materials, that is, the problem of being unable to achieve effective slippage due to the close stack of sheets and the existence of interaction forces, resulting in large cracks generated during the stretching process and make the sensors suffer from terrible stretchability.[42] Dong et al. incorporated one-dimensional material carbon nanotubes (CNTs) with MXene sheets to connect the conductive pathways that were blocked by cracks, which effectively enhanced the strain sensing range of the MXene/CNTs-based strain sensor, but this has not fundamentally solved the problem of effective slippage.[43] To realize effective slippage, it is necessary to reduce the stacking density of MXene sheets and reduce the interaction force between the


https://doi.org/10.1021/acsanm.5c01438
ACS Appl. Nano Mater. 2025, 8, 10022−10032

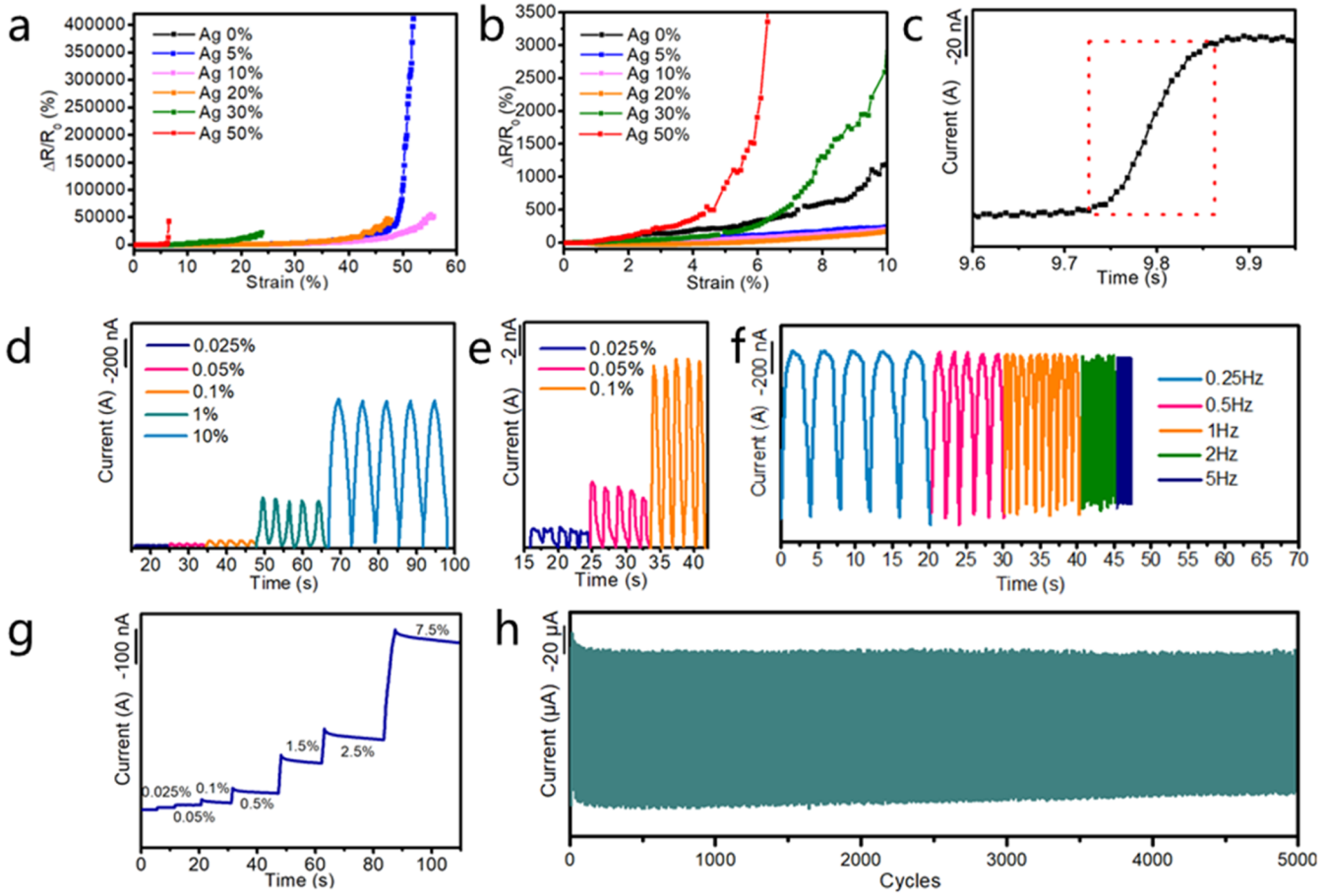


**Figure 2.** (a) Relative resistance−strain curves of $Ti_3C_2T_x$/Ag NPs film-based strain sensors with different Ag NPs content (the stretching rate was 60% $min^{-1}$). (b) Reproduce the curves in (a) within the strain range of 0−10%. (c) Response time test (the stretched strain was 1%), (d−e) cycling test under varying strains, (f) frequency response test, (g) detection limit test, and (h) cycle stability test of the strain sensor based on the $Ti_3C_2T_x/Ag_5$ composite film at 20% strain.

sheets. Then, inspired by the principle of the roller, we can legitimately speculate that the zero-dimensional materials with a regular spherical shape may play a certain role in lubricating and promoting effective slippage between the adjacent sheets.

Herein, we composited $Ti_3C_2T_x$ (a typical MXene material) sheets with silver nanoparticles (Ag NPs) to form a 0D-2D $Ti_3C_2T_x$/Ag NPs multidimensional composite network structure. Ag NPs entered into the interlayer of $Ti_3C_2T_x$ sheets to expand the interlayer distance and weaken the interaction force, which effectively promoted the effective slippage between $Ti_3C_2T_x$ sheets and enlarged the stain sensing range of sensors. Meanwhile, Ag NPs also increased the contact sites between different conductive sensitive elements, which greatly improved the sensitivity of sensors. The as-prepared strain sensor exhibited excellent comprehensive sensing performance, including extremely high sensitivity (greater than 153.28), wide strain sensing range (51.5%), low detection limit (0.025%), and good cycle stability (over 5000 times), reaching the performance index of the maximum strain induction range exceeding 50%, and the sensitivity was higher than 100 in the entire strain range. In addition, the strain sensor can be attached to different parts of the human body and perform real-time accurate monitoring of full-range human body motion, demonstrating promising prospects in practical applications.

## RESULTS AND DISCUSSION

Figure 1a demonstrates a facile fabrication process of the $Ti_3C_2T_x$/Ag NPs composite film. In detail, the $Ti_3C_2T_x$ sheets were prepared by a conventional wet etching method, that is, by using lithium fluoride (LiF) and hydrochloric acid (HCl) as etchants to selectively etch and remove the Al atomic layer in the raw material $Ti_3AlC_2$ to obtain multilayer products and subsequently using sonication to realize delamination. The morphology of the as-prepared $Ti_3C_2T_x$ sheets is shown in Figure 1d−e. The lateral size of the $Ti_3C_2T_x$ sheet was about 200−300 nm and the thickness was about 1−2 nm, indicating that the sheet was completely delaminated and the size distribution was relatively uniform. The Ag NPs were fabricated by using sodium borohydride ($NaBH_4$) to reduce silver nitrate ($AgNO_3$), in which sodium lauryl sulfate acted as a surfactant, and the size of Ag NPs can be adjusted by regulating the molar ratio of $AgNO_3$ and $NaBH_4$. When the molar ratio of $AgNO_3$ and $NaBH_4$ was 1:6, the morphology of the prepared Ag NPs can be seen in Figure 1c, which shows that the size of Ag NPs was very uniform, with an average diameter of about 10 nm. Afterward, a series of $Ti_3C_2T_x$/Ag NPs composite films can be fabricated by simply mixing $Ti_3C_2T_x$ sheets and Ag NPs in different proportions and a vacuum filtration process. For simplicity, we named the composite film $Ti_3C_2T_x/Ag_y$ according to the amount of Ag NPs incorporated, where y represents the mass fraction of Ag


https://doi.org/10.1021/acsanm.5c01438
ACS Appl. Nano Mater. 2025, 8, 10022−10032

NPs. As shown in Figure 1b, it was obvious that compared with the pure $Ti_3C_2T_x$ film, after the incorporation of Ag NPs, the characteristic peak of Ag (approximately 38°) appeared in the XRD pattern of the composite film, and the position of the characteristic peak corresponding to the (002) crystal plane of $Ti_3C_2T_x$ shifted from 7.04 to 6.45°. According to the Bragg formula, it was shown that the addition of Ag NPs significantly expanded the interlayer spacing between $Ti_3C_2T_x$ sheets, indicating that the Ag NPs successfully entered into the interlayer of the $Ti_3C_2T_x$ sheets and had a certain influence on the interaction between the adjacent sheets. Figure 1f–h and Figure S1 demonstrate the morphologies of the $Ti_3C_2T_x$/Ag NPs composite films with various amounts of Ag NPs. The surface of the pure $Ti_3C_2T_x$ film was relatively flat and contained some wrinkles with a small amplitude. When 5 wt % of Ag NPs was compounded with the $Ti_3C_2T_x$ sheet, the Ag NPs can be observed on the surface of the composite film obviously, and the wrinkles of the $Ti_3C_2T_x$ sheets increased and the undulation became larger. In addition, with the increase in the amount of Ag NPs incorporated, the density of Ag NPs in the composite film was continuously increased. In order to investigate the effect of the amount of Ag NPs on the interlayer distance of composite films, we observed the cross sections of composite films with different Ag NPs content. As shown in Figure S2, the cross-sectional SEM images of the composite films obtained when the Ag NPs were incorporated at 0, 5, and 30 wt % (note that the amount of $Ti_3C_2T_x$ used remains the same) can be found. The thicknesses of these films were 150, 240, and 310 nm, respectively, implying that the interlayer distance of the films increased with the increase in the amount of Ag NPs. And we can find that the Ag NPs did enter between the adjacent $Ti_3C_2T_x$ sheets uniformly, which effectively verified the XRD results.

In order to investigate the effect of the amount of Ag NPs incorporated on the sensing performance of flexible strain sensors, 5, 10, 20, 30, and 50 wt % Ag NPs were, respectively, compounded with a consistent amount of $Ti_3C_2T_x$ sheets. And each sample was assembled into a flexible strain sensor, whose sensing performance was tested and is shown in Figure 2a,b. The sensitivity of strain sensors can be evaluated by the slope of the relative resistance variation–strain curve, which is usually expressed by a Gauge Factor (GF); therefore, the value of GF can be calculated by GF = $(\Delta R/R_0)/\varepsilon$ ($R_0$ stands for the initial resistance, $\Delta R$ represents the difference between the resistance under a certain strain and the initial resistance, and $\varepsilon$ is strain).

It can be observed that when without the incorporation of Ag NPs, the strain sensor based on the pure $Ti_3C_2T_x$ film exhibited a very narrow strain sensing range of merely 11.83%, and it had a GF of 75.80 within the strain range of 0–8.76%, and a GF of 628.94 within the strain range of 8.76–11.17%. Then, the GF increased to 3160.50 when the strain sensor was stretched to a strain of 11.83%. The $\Delta R/R_0$-$\varepsilon$ curve of the sensor was relatively gentle in the early stage of stretching, the slope increased rapidly with the enlargement of strain, and the overall strain sensing range was very narrow, which were typical features of the strain sensors based on common two-dimensional sensitive materials. This unsatisfactory phenomenon can be explained by the fact that two-dimensional sheets cannot be effectively slipped during the stretching process due to the close stacking of the sheets and the presence of interaction forces between the adjacent sheets.

When a modicum of Ag NPs (5 wt %) was added, the maximum strain sensing range of the sensor reached 51.5%, which was about five times that of the pure $Ti_3C_2T_x$ film-based strain sensor. Thereinto, the GF in the strain range of 0–36.5% was as high as 153.28, and it rapidly increased to 2508.94 in the range of 36.5–49.05%, and 122311.87 in the range of 49.05–51.5%, successfully realizing the performance index that the maximum strain sensing range was greater than 50%, and the sensitivity was higher than 100 in the entire strain sensing range. It was plain as daylight that compared with the pure $Ti_3C_2T_x$ film-based strain sensor, the sensitivity and strain sensing range of the sensor based on the $Ti_3C_2T_x/Ag_5$ composite film had been greatly enhanced, especially the strain sensing range was enlarged about 5 times, indicating that Ag NPs had played a momentous role in promoting effective slippage between $Ti_3C_2T_x$ sheets and increased sensitive sites to improve sensitivity. In addition, Table S1 shows the sensing performance of the $Ti_3C_2T_x/Ag_5$ composite film-based sensor compared with the currently reported strain sensor, and it was obvious that strain sensors based on other pure materials also cannot achieve high sensitivity and wide sensing range, further indicating the superiority of the $Ti_3C_2T_x$/Ag NPs multidimensional composite network structure. When the amount of Ag NPs was increased to 10 wt %, the strain sensing range of the sensor reached 55.28%, and its sensitivity reached 72.57, 598.08, and 4128.58 within the strain ranges of 0–31.37, 31.37–45.62, and 45.62–55.28%, respectively. In comparison with the $Ti_3C_2T_x/Ag_5$-based sensor, the strain sensing range of the sensor was slightly increased, but the sensitivity was diminished. This result may be due to the excessive addition of 10 wt % Ag NPs, which expanded the interlayer distance of $Ti_3C_2T_x$ sheets and facilitated the effective slippage of adjacent sheets to enhance the strain sensing range. But at the same time, the weakening of the interaction between the $Ti_3C_2T_x$ sheets makes the conductive network less susceptible to damage during stretching, so that the response of the variation in relative resistance will become smaller. However, as the amount of Ag NPs further increased to 20, 30, and 50 wt %, the maximum strain sensing range of the corresponding strain sensors gradually decreased to 47.53, 23.76, and 6.50%, which may be a result of the fact that the excessive incorporation of Ag NPs increased the brittleness of the composite film and make the film easily break under tensile strain, so the sensing performance deteriorated sharply. In summary, we can find that when the amount of Ag NPs was 5 wt %, the comprehensive performance of the sensor was the best, followed by the sensor where the amount of Ag NPs was 10 wt %. As shown in Figure 2b and Table S2, the $\Delta R/R_0$-$\varepsilon$ curves of the strain sensors based on $Ti_3C_2T_x/Ag_5$ and $Ti_3C_2T_x/Ag_{10}$ films within a small strain range exhibited a more excellent linearity than the other curves. Furthermore, three independent experiments were conducted on the same $Ti_3C_2T_x/Ag_5$ films and different batches of $Ti_3C_2T_x/Ag_5$ films under the same conditions were tested (Figure S3). It can be seen that the relative resistance–strain curves were highly coincident, indicating the reliability and repeatability of the experiments. In short, the appropriate proportion of Ag NPs in the $Ti_3C_2T_x$ sheets was able to endow the strain sensor with high sensitivity and a strain sensing range simultaneously.

In addition, taking the $Ti_3C_2T_x/Ag_5$ composite film as a research object, we also measured other sensing performances of the strain sensor based on the $Ti_3C_2T_x$/Ag NPs multidimensional composite network structure. Figure 2c shows the


https://doi.org/10.1021/acsanm.5c01438
ACS Appl. Nano Mater. 2025, 8, 10022–10032

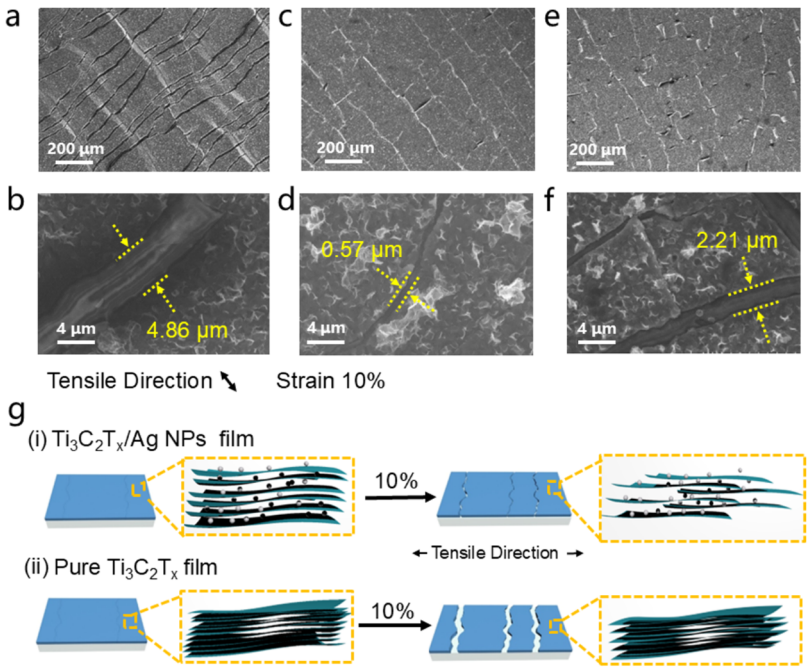


**Figure 3.** (a and b) Pure $Ti_3C_2T_x$ film, (c and d) $Ti_3C_2T_x/Ag_5$ film, and (e, f) $Ti_3C_2T_x/Ag_{30}$ film-based strain sensors were initially stretched to 10%. (g) Schematic diagram of the sensing mechanism of the $Ti_3C_2T_x/Ag_5$ film and Pure $Ti_3C_2T_x$ film-based strain sensors.

real-time response I−t curve of the sensor under a small strain of 1%, revealing that the response time of the sensor was 138 ms, which can adequately satisfy the requirements of real-time monitoring of human body movements. As shown in Figure 2d−e, the sensor was cycled 5 times at strains of 0.025, 0.05, 0.1, 1.0, and 10%, respectively, with a stretching rate of 60% $min^{-1}$ (0.1 mm/s). Under the minimum strain of 0.025%, the response curve can also achieve stable periodic regularity, indicating that the detection limit of the sensor was as low as 0.025%, and it had very high sensitivity under small strain, which was sufficient to meet most human body detection of subtle deformations. As shown in Figure 2g, the experimental results were further verified through the step strain response curve, that is, the variation curve of the current as the step strain increased from 0.025 to 7.5%. Figure 2f demonstrates the frequency response of the strain sensor at a frequency of 0.25−5 Hz at a strain of 10%, proving that the sensor was capable of achieving real-time high-frequency response and the shape and amplitude of the current signal peaks at different selected frequencies remain the same. In addition, as shown in Figures 2h, S4 and S5, after 5000 stretching releasing cycles under different strains (10−30%), the current signal intensity of the sensor had almost no attenuation, indicating that the sensor had excellent cycling and mechanical stability. Additionally, the strain sensor that had been tested before was placed at room temperature for one month, and then a relative resistance change−strain test was conducted. It was found that the test curves were highly overlapped, indicating the durability of the sensor in practical applications (Figure S6). Moreover, when the $Ti_3C_2T_x/Ag_5$ composite film was placed at different temperatures (15−35 °C), it was also found that the test curves were highly overlapped, indicating the reliability of the sensor in practical applications (Figure S7). We can conclude that the strain sensor based on the $Ti_3C_2T_x$/Ag NPs multidimensional composite network structure exhibited superior comprehensive performance, including a high sensitivity, a wide sensing range, a low detection limit, good cycling stability, and so on.

In order to investigate the sensing mechanism of the $Ti_3C_2T_x$/Ag NPs multidimensional composite network structure to confirm the effect of Ag NPs on the sensing performance, we observed the variations in the morphology of the $Ti_3C_2T_x$/Ag NPs composite films with varying contents of Ag NPs during the first stretching/releasing cycle. Figure 3, respectively, demonstrates the morphologies of the pure $Ti_3C_2T_x$ film, $Ti_3C_2T_x/Ag_5$ film, and $Ti_3C_2T_x/Ag_{30}$ film-based strain sensors when they are initially stretched to a certain strain of 10%. It can be seen in Figure 3c,d that abundant microcracks were arranged on the surface of the $Ti_3C_2T_x/Ag_5$ composite films perpendicular to the tensile direction, and the average crack width was about 0.57 $\mu$m.

As shown in Figure 3a,b,e,f, the pure $Ti_3C_2T_x$ film without Ag NPs being incorporated and the composite film with 30 wt % Ag NPs also generated ordered cracks perpendicular to the tensile direction at 10% strain. However, it can be found that the widths of the cracks of the pure $Ti_3C_2T_x$ film and $Ti_3C_2T_x/Ag_{30}$ composite film were about 4.86 and 2.21 $\mu$m, respectively, which were much larger than that of the $Ti_3C_2T_x/Ag_5$ composite film explicitly. Moreover, it can be observed in Figure 3e that the $Ti_3C_2T_x/Ag_{30}$ composite film was more brittle than the other two samples, the integrity of the film was worse, and the phenomenon of breaking and peeling could possibly occur during the stretching process. The difference in morphology of $Ti_3C_2T_x$/Ag NPs multidimensional composite films with various Ag NPs content confirmed our previous conjecture that the incorporation of an appropriate amount of Ag NPs can effectively promote the effective slippage between $Ti_3C_2T_x$ sheets, play a lubricating effect, and inhibit the cracks from propagation. However, the addition of excessive Ag NPs will increase the brittleness of the composite film, which was not conducive to the enhancement of sensing performance.


https://doi.org/10.1021/acsanm.5c01438
ACS Appl. Nano Mater. 2025, 8, 10022−10032

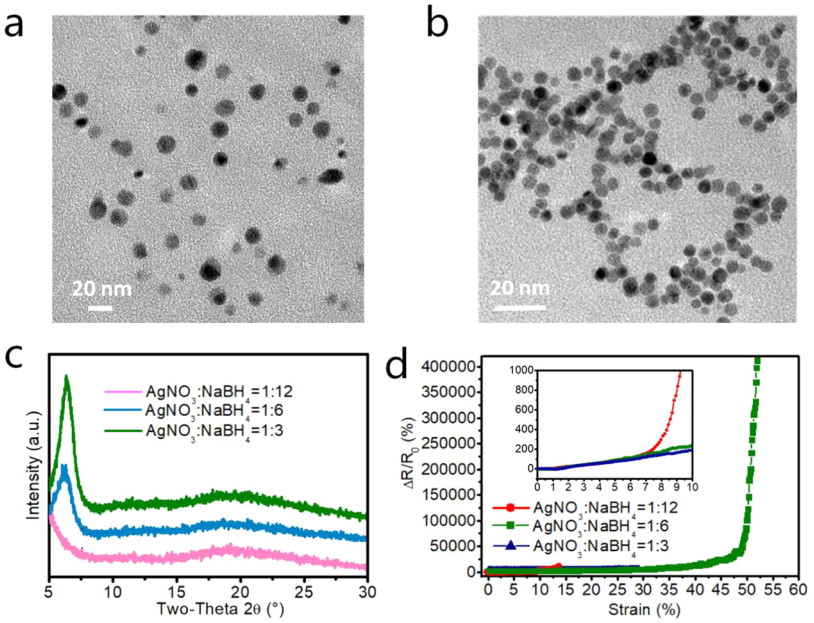


**Figure 4.** TEM images of Ag NPs prepared when the molar ratio of $AgNO_3$ and $NaBH_4$ was (a) 1:12 and (b) 1:3. (c) XRD patterns of $Ti_3C_2T_x$/Ag NPs films with different Ag NPs sizes. (d) Relative resistance−strain curves of $Ti_3C_2T_x$/Ag NPs-based strain sensors with different sizes of Ag NPs.

The variation in morphology of the $Ti_3C_2T_x/Ag_5$ film during the complete stretching process is shown in Figure S8. As shown in Figure S8a,b, when no tensile strain was applied, there were some microcracks present on the surface of the $Ti_3C_2T_x/Ag_5$ conductive composite film, which was mainly due to the ceramic nature of $Ti_3C_2T_x$. Even if $Ti_3C_2T_x$ belonged to two-dimensional materials, it had a certain degree of brittleness, leading to certain damage to the thin film structure and the generation of microcracks during the film preparation and sensor manufacturing process. In addition, it was obvious that Ag NPs were uniformly distributed around the $Ti_3C_2T_x$ sheets. When a small strain of 10% was applied, as shown in Figure S8c,d, the presence of Ag NPs and the generation of ordered microcracks made the sensor have a high sensitivity of 153.28. Afterward, the $Ti_3C_2T_x/Ag_5$ composite film was further stretched to a strain of 30% (Figure S8e,f), and the sensitivity to microcracks increased significantly. The microcracks spread along the direction perpendicular to the applied tensile strain, and the crack width was close to 1.71 $\mu$m. The crack expanded the nonconductive area, resulting in an increase in resistance. Ag NPs migrated toward the crack tip to form a local conductive bridge, which helped to delay the complete fracture. When it was stretched to 50% strain (Figure S8g,h), it can be explicitly found that the microcracks of the film were gradually propagated and the widths of the cracks reached 6.71 $\mu$m. This led to the loss of the conductive bridging function provided by Ag NPs. The conductive pathways of the film were gradually blocked by cracks, and the resistance rapidly increased until the film lost conductivity; therefore, the sensitivity of the sensor also rapidly increased to the order of $10^6$ during this strain range, which was in line with the common crack propagation mechanism of two-dimensional materials. Finally, after the tensile stress was released, the cracks in the film were recovered, ensuring the cyclic stability of the sensor.

The morphological changes of the pure $Ti_3C_2T_x$-based strain sensor and $Ti_3C_2T_x/Ag_{30}$-based strain sensor under different strains during the complete stretching/releasing process are shown in Figures S9 and S10. By contrast, the $Ti_3C_2T_x$ film was relatively intact in the stretching process, but the width of the ordered cracks was larger under the same strain, which can be attributed to the high stacking density and strong interaction of $Ti_3C_2T_x$ sheets, causing ineffective slippage of adjacent sheets. However, the $Ti_3C_2T_x/Ag_{30}$ composite film exhibited cracking and peeling in many places before stretching. The overall brittleness was larger, and cracks with varying widths appeared during stretching. However, the average width of cracks was smaller than that of the pure $Ti_3C_2T_x$ film, indicating that the Ag NPs indeed played an important role in promoting the slippage of the $Ti_3C_2T_x$ sheets to reduce crack propagation, but its brittleness had a severe impact on the sensing performance. In conclusion, in the $Ti_3C_2T_x$/Ag NPs multidimensional composite network structure, the $Ti_3C_2T_x$ sheets provide a layered structure, which endows the strain sensor with high sensitivity through the generation and propagation of cracks. The addition of a proper amount of Ag NPs can not only effectively promote slippage of adjacent sheets and inhibit crack growth to increase the strain sensing range of the sensor but also increase the sensitivity sites and increase the variation in the conductive network through migration to further improve the sensitivity of the sensor. The highly efficient synergistic interaction of $Ti_3C_2T_x$ sheets and Ag NPs provides the strain sensor with excellent comprehensive sensing performance.

In addition, the effect of different Ag NPs sizes on the performance of the strain sensors based on the $Ti_3C_2T_x$/Ag NPs multidimensional composite structure was also investigated. As mentioned above, the size of Ag NPs can be regulated by controlling the molar ratio of $AgNO_3$ and $NaBH_4$. As shown in Figures 1c and 4a,b, when the molar ratios of $AgNO_3$ and $NaBH_4$ were respectively 1:12, 1:6, and 1:3, the diameters of the as-prepared Ag NPs are approximately 15−20, 10, and 5 nm, respectively. It can be found that as the amount of $AgNO_3$ added to $NaBH_4$ increased, the particle size of the Ag NPs gradually decreased. And among them, when the molar ratio of $AgNO_3$ and $NaBH_4$ was 1:12, the size of the obtained


https://doi.org/10.1021/acsanm.5c01438
ACS Appl. Nano Mater. 2025, 8, 10022−10032

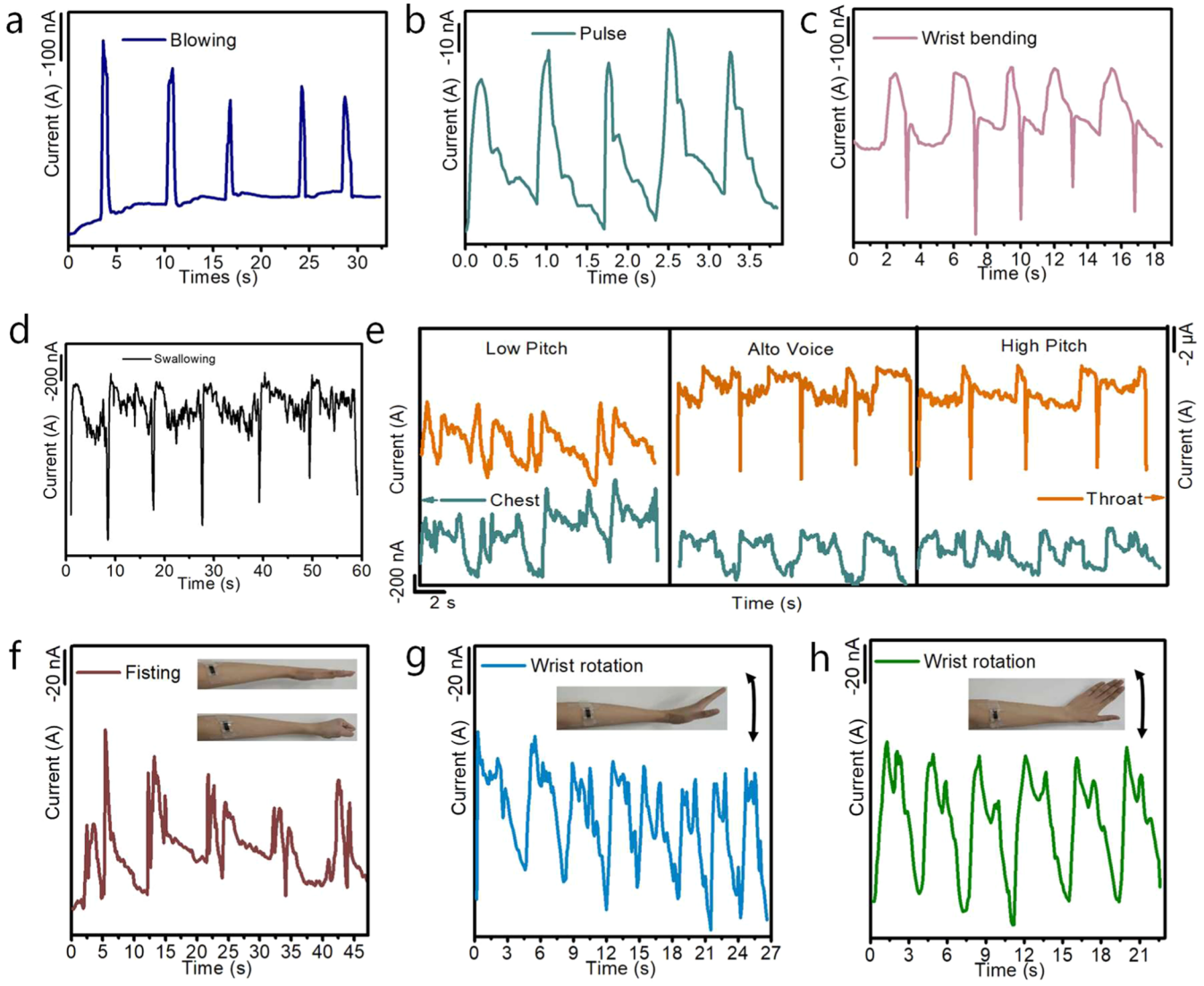


**Figure 5.** Human physiological signal display of a $Ti_3C_2T_x$/Ag NPs-based strain sensor. (a) Blowing, (b) pulse, (c) wrist rotation, (d) swallowing, (e) voice recognition, (f) fisting, (g) wrist back and forth rotation, and (h) wrist left and right rotation.

silver nanoparticles was very uneven, but the size distribution of the Ag NPs obtained in the other two cases was relatively uniform. Moreover, the dispersion and diameter distribution of the synthesized silver nanoparticles in the solution hydrodynamic environment were measured by the dynamic light scattering method (Figure S11). When the molar ratios of $AgNO_3$ and $NaBH_4$ were 1:6 and 1:3, respectively, the synthesized silver nanoparticles were uniform and had good dispersion. When the molar ratio of $AgNO_3$ to $NaBH_4$ was 1:12, the synthesized silver nanoparticles had uneven sizes and better dispersibility than the former. It was consistent with the previous idea. Ag NPs with different diameters were incorporated into the $Ti_3C_2T_x$ sheets in a mass fraction of 5 wt %, respectively. For the sake of simplicity, the composite films incorporated with Ag NPs of different particle sizes were named $Ti_3C_2T_x$/Ag $NPs_{1:12}$, $Ti_3C_2T_x$/Ag $NPs_{1:6}$, and $Ti_3C_2T_x$/Ag $NPs_{1:3}$, respectively, according to different molar ratios of $AgNO_3$ and $NaBH_4$. The XRD patterns of $Ti_3C_2T_x$/Ag NPs composite films with different Ag NPs sizes are demonstrated in Figure 4c. The results showed that when the mixed amount of $AgNO_3$ increased, that is, when the diameters of the Ag NPs gradually decreased, the position of the characteristic peak corresponding to the (002) crystal plane of $Ti_3C_2T_x$ in the composite film was less than 5, 6.055, and 6.407°, respectively, indicating that the interlayer distance of the composite film was gradually increasing; that is, the larger the particle diameter of the incorporated Ag NPs, the larger the interlayer distance of the film was. It was further confirmed that the Ag NPs entered into the interlayer of the $Ti_3C_2T_x$ sheets and played a role in reducing the sheet stacking density and the interaction force between the adjacent sheets. The sensing performance of the strain sensors based on $Ti_3C_2T_x$/Ag NPs composite films with different diameters of Ag NPs was evaluated in Figure 4d. When the molar ratio of $AgNO_3$ and $NaBH_4$ was 1:12, that is, the size of the Ag NPs was about 15−20 nm, the strain sensing range of the prepared strain sensor was only 13.86%, among which the GF was 23.45 in the strain range of 0−7.48%, 292.45 in the strain range of 7.48−8.69%, and increased to 1666.16 in the strain range of 8.69−13.86%. The comprehensive sensing performance was not desirable, which may have contributed to the uneven size of Ag NPs, and the larger size of Ag NPs may excessively weaken the interaction between $Ti_3C_2T_x$ sheets, resulting in a loose film structure. The sensitivity and strain sensing range of the $Ti_3C_2T_x$/Ag $NPs_{1:6}$-based strain sensor


https://doi.org/10.1021/acsanm.5c01438
ACS Appl. Nano Mater. 2025, 8, 10022−10032

were analyzed before; that is, the GF value was 153.28−122311.87 with the entire strain sensing range of 0−51.5%, which was greatly improved compared with the former. When the amount of $AgNO_3$ further increased to 1:3, that is, the size of the Ag NPs decreased to about 5 nm, the maximum strain sensing range of the strain sensor reached 28.50%, and the GF was 3.16, 22.94, and 90.99 between 0 and 1.0%, 1.0−10.71%, and 10.71−28.50, respectively. It was evident that the sensitivity and strain sensing range of this sensor were far from those of the sensor with Ag NPs size of 10 nm, which may be due to the size of Ag NPs being too small to effectively promote the mutual slippage between the $Ti_3C_2T_x$ sheets. Therefore, for $Ti_3C_2T_x$ sheets with a lateral size of about 200−300 nm, Ag NPs with a diameter of 10 nm were appropriate to produce highly effective synergy with them and endowed the strain sensors with high sensing performance.

In view of the flexible strain sensor based on the $Ti_3C_2T_x$/Ag NPs multidimensional composite network structure with high sensitivity, wide strain sensing range, low detection limit, and other high performance, we attached the sensor to each part of the human body and various real-time physiological signal detections were performed. As shown in Figure 5a, we placed the sensor on a flat surface and blew the surface of the sensor intermittently at a distance of 10 cm from the plane. It was found that the obtained $I-T$ response curve showed a regular periodic change, indicating that the sensor was able to monitor the changes in air flow and realize noncontact sensing. As shown in Figure 5b, we attached the strain sensor to the inside of the wrist to capture the pulse signal and found that the curve of each response cycle had three clear characteristic peaks, which represented percussion (P), tidal (T), and diastolic pressure (D) respectively, indicating that the sensor can accurately detect the physiological signals with minimal deformation. When the strain sensor was attached to the throat, a response curve corresponding to a swallowing process was precisely recorded. And due to the high sensitivity and low detection limit, the strain sensor can accurately identify high pitch, alto voice, and low pitch, and the shape and intensity of the current signals generated by attaching the sensor to the throat and chest cavity, respectively, were different, resulting from that when sounds of different frequencies were emitted, the vibration-inducing parts and the vibration intensity were different, which made the strain senor be promising for finding the correct sound position. For example, when the low-pitch sound, the vibration of the chest cavity was the most obvious, so the intensity of the response signal was the largest. In order to detect the physiological signal with large deformation, as shown in Figure 5c, we attached the sensor to the wrist to collect the electrical signal when the wrist performed periodic bending movements. It can be found that the current signal of the sensor changes periodically with the wrist flexion, and the characteristic peaks of each cycle remain the same, indicating that the sensor can also meet the requirement of monitoring a wide-range motion of the human body. Moreover, as shown in Figure 5g,h, we applied the sensor to the pronator circular muscle of the forearm, performing fists, wrist back and forth, and wrist left and right rotation, respectively. It was found that the sensor can present different characteristic signals for different actions, revealing that the sensor can accurately distinguish different actions of the same muscle, which can be used for human body posture correction, etc., and has a high practical application value.

## CONCLUSIONS

We have designed a unique $Ti_3C_2T_x$/Ag NPs multidimensional composite network structure by incorporating Ag NPs as the second phase to the $Ti_3C_2T_x$ sheets. The Ag NPs entered into the interlayer of $Ti_3C_2T_x$ sheets, which effectively expanded the interlayer distance between the sheets to reduce the stacking density and interaction force between the $Ti_3C_2T_x$ sheets and promote effective slippage of the $Ti_3C_2T_x$ sheets. The interlayer distance increased as the content and size of Ag NPs increased, which showed an important influence on the sensing performance of $Ti_3C_2T_x$/Ag NPs-based strain sensors. When the size of the Ag NPs was 10 nm and the content was 5 wt %, the prepared sensor exhibited excellent comprehensive sensing performance, including extremely high sensitivity (greater than 153.28 within the entire sensing range), a wide strain sensing range (51.5%), a very low detection limit (0.025%), and good cycle stability (more than 5000 times), effectively illustrating the great promotion effect of appropriate content and size of Ag NPs can on the sensing performance of strain sensors. The construction of this multidimensional composite structure provides inspiration for solving the problem that two-dimensional sensitive materials cannot achieve effective slippage due to the close stacking of sheets and the existence of interaction forces.

## EXPERIMENT SECTION

**Materials.** $Ti_3AlC_2$ was purchased from Forsman Scientific (Beijing, Co., Ltd.). Hydrochloric acid (HCl), Lithium fluoride (LiF), and sodium dodecyl sulfate (SDS) were purchased from China National Medicines Corporation Ltd. Sodium borohydride ($NaBH_4$) was purchased from Sigma-Aldrich, and silver nitrate ($AgNO_3$) was purchased from Alfa Aesar (Shanghai, Co., Ltd.).

**Synthesis of $Ti_3C_2T_x$ Suspension.** First, 2 g of LiF was immersed in 23 mL of 9 M HCl and stirred for 10 min, which was followed by adding 1 g of $Ti_3AlC_2$ powder into the mixed solution, and the mixture was magnetically stirred in an oil bath at 60 °C $Ti_3C_2T_x$ for 48 h. Then, the as-prepared paste was repeatedly rinsed with deionized water several times until the pH value was over 6 and was dried by freeze-drying to obtain multilayer (m-$Ti_3C_2T_x$). The m-$Ti_3C_2T_x$ was dispersed into deionized water with the ratio of 1 g:100 mL and was sonicated for 1 h under flowing Ar. Then, the delaminated product was centrifuged for 1 h at 3500 rpm to collect the upper suspension and was dried in a frozen drying oven. Finally, the as-obtained $Ti_3C_2T_x$ floccule was redispersed in water to prepare a $Ti_3C_2T_x$ solution with a concentration of 1 mg/mL.

**Synthesis of Silver Nanoparticles (Ag NPs).** 10 mmol $AgNO_3$ powder and 0.1 mol of SDS powder were immersed in 10 mL of deionized and magnetically stirred for 30 min (1560 rmp), and 30 mL of 2.0 mM $NaBH_4$ aqueous solution was also prepared. Then, 5, 10, and 15 mL of the mixture solution of $AgNO_3$ and SDS were, respectively, added into NaBH4 aqueous solution drop by drop in an ice bath. The as-prepared light yellow suspension was a Ag NPs suspension with a concentration of 0.0135−0.0405 mg/mL.

**Fabrication of the $Ti_3C_2T_x$/Ag NPs Composite Film.** The $Ti_3C_2T_x$ suspension was added into the Ag NPs suspension at a mass fraction of 5−50 wt % and continuously stirred for 3 h. Then, the mixture was vacuum filtered to


https://doi.org/10.1021/acsanm.5c01438
ACS Appl. Nano Mater. 2025, 8, 10022−10032

fabricate a composite and dried in a vacuum oven for 12 h at room temperature.

**Fabrication of $Ti_3C_2T_x$/Ag NPs Composite Film-Based Strain Sensors.** The fabrication of $Ti_3C_2T_x$/Ag NPs composite film-based strain sensors has been presented in previous work. The as-resulted composited film was cut into rectangles with a size of 0.6 × 2.0 cm and was transferred to a prepolymerized polydimethylsiloxane (PDMS, Dow Corning) substrate. A dimethylsiloxane monomer and cross-linking agent were mixed at a mass ratio of 10:1, magnetically stirred for 20 min, and placed in a vacuum oven for 10 min to remove bubbles. Afterward, PDMS was poured into a cuboid mold that was 80 × 15 × 1 mm and then was prepolymerized at 80 °C for 10 min. The tailored conductive film was transferred to prepolymerized PDMS with the conductive material downward. Then, the sample was placed in a drying oven at 80 °C for 1 h to finish the polymerization reaction of PDMS. The filter membrane coated on the conductive material was dissolved with acetone in 30 min. Finally, silver electrodes were coated on both ends of the $Ti_3C_2T_x$ rectangle to complete the fabrication of the $Ti_3C_2T_x$-based strain sensors.

**Characterization.** The phase composition and crystalline structure of the samples were analyzed by a high-resolution multifunction X-ray diffractometer (D8 Discover Davinci, German). The morphologies were characterized by a field emission scanning electron microscope (S-4800, Hitachi, Japan). The concentration of the $Ti_3C_2T_x$ suspension was calibrated using an ultraviolet−visible spectrophotometer (PerkinElmer Lambda 950). The size distribution of the $Ti_3C_2T_x$ suspension was obtained by atomic force microscopy (NTEGRA, NT-MDT, Russia). The strain sensing tests were conducted by applying a high-precision electronic universal testing machine (CMT6103, MTS Systems, China) with a tensile controller and a software system. The resistance variation was determined by using an electrochemical workstation (PARSTAT 2273, Princeton Applied Research) by applying a constant voltage (0.1 V) on the two sides of the strain sensor to obtain a real-time current signal.

## ■ ASSOCIATED CONTENT

### Supporting Information

The Supporting Information is available free of charge at https://pubs.acs.org/doi/10.1021/acsanm.5c01438.

The additional SEM characterization and experimental details of all materials are shown in Figures S1 to S11 (PDF)

## ■ AUTHOR INFORMATION


### Corresponding Authors

**Yucai Shen** − *College of Material Science and Engineering, Nanjing Tech University, Nanjing 211816, China*; Email: ycshen@njtech.edu.cn

**Yin Cheng** − *State Key Laboratory of High Performance Ceramics and Superfine Microstructure, Shanghai Institute of Ceramics, Chinese Academy of Sciences, Shanghai 200050, China*; orcid.org/0000-0001-7647-3558; Email: chengyin@mail.sic.ac.cn

### Authors

**Jintao Zhang** − *College of Material Science and Engineering, Nanjing Tech University, Nanjing 211816, China*

**Yina Yang** − *State Key Laboratory of High Performance Ceramics and Superfine Microstructure, Shanghai Institute of Ceramics, Chinese Academy of Sciences, Shanghai 200050, China*

**Ranran Wang** − *State Key Laboratory of High Performance Ceramics and Superfine Microstructure, Shanghai Institute of Ceramics, Chinese Academy of Sciences, Shanghai 200050, China*; orcid.org/0000-0001-5097-2834

**Jing Sun** − *State Key Laboratory of High Performance Ceramics and Superfine Microstructure, Shanghai Institute of Ceramics, Chinese Academy of Sciences, Shanghai 200050, China*; orcid.org/0000-0003-1101-1584

**Liangjing Shi** − *State Key Laboratory of High Performance Ceramics and Superfine Microstructure, Shanghai Institute of Ceramics, Chinese Academy of Sciences, Shanghai 200050, China*

Complete contact information is available at: https://pubs.acs.org/10.1021/acsanm.5c01438

### Author Contributions

§J.Z. and Y.Y. contributed equally to this work.


### Notes

The authors declare no competing financial interest.

## ■ ACKNOWLEDGMENTS

This work was financially supported by the National Natural Science Foundation of China (52203365, 62471459), the Shanghai Rising Star Program (24QA2710600), and the Shanghai Science and Technology Commission Project (23520711000).

## ■ REFERENCES


(1) Gao, L.; Hu, B. L.; Wang, L. P.; Cao, J. W.; He, R.; Zhang, F. Y.; Wang, Z. M.; Xue, W. H.; Yang, H. L.; Li, R. W. Intrinsically elastic polymer ferroelectric by precise slight cross-linking. *Science* **2023**, *381* (6657), 540−544.

(2) Li, H.; Chen, J. W.; Chang, X. H.; Xu, Y. Q.; Zhao, G. Y.; Zhu, Y. T.; Li, Y. J. A highly stretchable strain sensor with both an ultralow detection limit and an ultrawide sensing range. *J. Mater. Chem. A* **2021**, *9* (3), 1795−1802.

(3) Li, L. H.; Zheng, Z.; Ge, C. L.; Wang, Y. F.; Dai, H.; Li, L. L.; Wang, S. Q.; Gao, Q.; Liu, M. Y.; Sun, F. Q.; Zhang, T. A Flexible Tough Hydrovoltaic Coating for Wearable Sensing Electronics. *Adv. Mater.* **2023**, *35* (40), No. 202304099.

(4) Shi, X.; Chen, P. N.; Peng, H. S. Making large-scale, functional, electronic textiles. *Nature* **2021**, *591* (7849), 240−245.

(5) Wang, L.; Luo, M. Q.; Zhang, Z. H.; Ji, D.; Chang, X. H.; Zhu, Y. T. Ultra-stretchable, robust, self-healable conductive hydrogels enabled by the synergistic effects of hydrogen bonds and ionic coordination bonds toward high-performance e-skins. *Chem. Eng. J.* **2024**, *500*, No. 156800.

(6) Chen, L. R.; Chang, X. H.; Chen, J. W.; Zhu, Y. T. Ultrastretchable, Antifreezing, and High-Performance Strain Sensor Based on a Muscle-Inspired Anisotropic Conductive Hydrogel for Human Motion Monitoring and Wireless Transmission. *ACS Appl. Mater. Interfaces* **2022**, *14* (38), 43833−43843.

(7) Wang, T.; Qiu, Z. G.; Li, H. C.; Lu, H.; Gu, Y. F.; Zhu, S. M.; Liu, G. S.; Yang, B. R. High Sensitivity, Wide Linear-Range Strain Sensor Based on MXene/Ag NW Composite Film with Hierarchical Microcrack. *Small* **2023**, *19*, No. 2304033.

(8) Zhu, G. X.; Li, H.; Peng, M. L.; Zhao, G. Y.; Chen, J. W.; Zhu, Y. T. Highly-stretchable porous thermoplastic polyurethane/carbon nanotubes composites as a multimodal sensor. *Carbon* **2022**, *195*, 364−371.

(9) Park, B.; Lee, Y.; Jung, W.; Scott, D. K.; Aalto, D.; Chung, H. J.; Kim, T. I. Deterministically assigned directional sensing of a nanoscale crack based pressure sensor by anisotropic Poisson ratios of the substrate. *J. Mater. Chem. C* **2021**, *9* (15), 5154−5161.
(10) Wang, L.; Xu, X. Y.; Chen, J.; Su, W. G.; Zhang, F.; Li, A. Q.; Li, C.; Xu, C. H.; Sun, Y. Crack Sensing of Cardiomyocyte Contractility with High Sensitivity and Stability. *ACS Nano* **2022**, *16*, 12645−12655.
(11) Deng, S. J.; Zhang, K. L.; Xie, D.; Zhang, Y.; Zhang, Y. Q.; Wang, Y. D.; Wu, J. B.; Wang, X. L.; Fan, H. J.; Xia, X. H.; Tu, J. P. High-Index-Faceted $Ni_3S_2$ Branch Arrays as Bifunctional Electrocatalysts for Efficient Water Splitting (vol 11, 12, 2019). *Nano-Micro Lett.* **2021**, *13* (1), No. 16.
(12) Wang, H.; Mao, Y. Y.; Ji, D.; Wang, L.; Wang, L.; Chen, J. W.; Chang, X. H.; Zhu, Y. T. Transparent, self-adhesive, highly environmental stable, and water-resistant ionogel enabled reliable strain/temperature sensors and underwater communicators. *Chem. Eng. J.* **2023**, *471*, No. 144674.
(13) Wu, S.; Moody, K.; Kollipara, A.; Zhu, Y. Highly Sensitive, Stretchable, and Robust Strain Sensor Based on Crack Propagation and Opening. *ACS Appl. Mater. Interfaces* **2023**, *15* (1), 1798−1807.
(14) Rim, Y. S.; Bae, S.-H.; Chen, H.; De Marco, N.; Yang, Y. Recent Progress in Materials and Devices toward Printable and Flexible Sensors. *Adv. Mater.* **2016**, *28* (22), 4415−4440.
(15) Amjadi, M.; Kyung, K. U.; Park, I.; Sitti, M. Stretchable, Skin-Mountable, and Wearable Strain Sensors and Their Potential Applications: A Review. *Adv. Funct. Mater.* **2016**, *26* (11), 1678−1698.
(16) Park, S.; Kim, H.; Kim, J. H.; Yeo, W. H. Advanced Nanomaterials, Printing Processes, and Applications for Flexible Hybrid Electronics. *Materials* **2020**, *13* (16), No. 3587.
(17) Shi, X. L.; Wang, H. K.; Xie, X. T.; Xue, Q. W.; Zhang, J. Y.; Kang, S. Q.; Wang, C. H.; Liang, J. J.; Chen, Y. S. Bioinspired Ultrasensitive and Stretchable MXene-Based Strain Sensor via Nacre-Mimetic Microscale "Brick-and-Mortar" Architecture. *ACS Nano* **2019**, *13* (1), 649−659.
(18) Yang, Y. N.; Cao, Z. R.; He, P.; Shi, L. J.; Ding, G. Q.; Wang, R. R.; Sun, J. $Ti_3C_2T_x$ MXene-graphene composite films for wearable strain sensors featured with high sensitivity and large range of linear response. *Nano Energy* **2019**, *66*, No. 104134.
(19) Yang, Y. N.; Shi, L. J.; Cao, Z. R.; Wang, R. R.; Sun, J. Strain Sensors with a High Sensitivity and a Wide Sensing Range Based on a $Ti_3C_2T_x$ (MXene) Nanoparticle-Nanosheet Hybrid Network. *Adv. Funct. Mater.* **2019**, *29* (14), No. 1807882.
(20) Wang, J.; Liu, L.; Yang, C.; Zhang, C.; Li, B.; Meng, X.; Ma, G.; Wang, D.; Zhang, J.; Niu, S.; Zhao, J.; Han, Z.; Yao, Z.; Ren, L. Ultrasensitive, Highly Stable, and Flexible Strain Sensor Inspired by Nature. *ACS Appl. Mater. Interfaces* **2022**, *14* (14), 16885−16893.
(21) Li, A. L.; Chen, Q. X.; Wang, P. P.; Gan, Y.; Qi, T. L.; Wang, P.; Tang, F. D.; Wu, J. Z.; Chen, R.; Zhang, L. Y.; Gong, Y. P. Ultrahigh-Sensitive Broadband Photodetectors Based on Dielectric Shielded $MoTe_2$/Graphene/$SnS_2$ p-g-n Junctions. *Adv. Mater.* **2019**, *31* (6), No. 1805656.
(22) Zhang, C.; Sun, J. N.; Lu, Y.; Liu, J. S. Nanocrack-based strain sensors. *J. Mater. Chem. C* **2021**, *9* (3), 754−772.
(23) Cao, Z. R.; Wang, R. R.; He, T. Y.; Xu, F. F.; Sun, J. Interface-Controlled Conductive Fibers for Wearable Strain Sensors and Stretchable Conducting Wires. *ACS Appl. Mater. Interfaces* **2018**, *10* (16), 14087−14096.
(24) Guo, X. H.; Hong, W. Q.; Zhao, Y. N.; Zhu, T.; Liu, L.; Li, H. J.; Wang, Z. W.; Wang, D. D.; Mai, Z. H.; Zhang, T. X.; Yang, J. Y.; Zhang, F. Z.; Xia, Y.; Hong, Q.; Xu, Y. H.; Yan, F.; Wang, M.; Xing, G. Z. Bioinspired Dual-Mode Stretchable Strain Sensor Based on Magnetic Nanocomposites for Strain/Magnetic Discrimination. *Small* **2023**, *19* (1), No. 202205316.
(25) Sun, H. L.; Dai, K.; Zhai, W.; Zhou, Y. J.; Li, J. W.; Zheng, G. Q.; Li, B.; Liu, C. T.; Shen, C. Y. A Highly Sensitive and Stretchable Yarn Strain Sensor for Human Motion Tracking Utilizing a Wrinkle-Assisted Crack Structure. *ACS Appl. Mater. Interfaces* **2019**, *11* (39), 36052−36062.
(26) Tian, Y.; Huang, M. J.; Wang, Y. L.; Zheng, Y. J.; Yin, R.; Liu, H.; Liu, C. T.; Shen, C. Y. Ultra-stretchable, sensitive and breathable electronic skin based on TPU electrospinning fibrous membrane with microcrack structure for human motion monitoring and self-powered application. *Chem. Eng. J.* **2024**, *480*, No. 147899.
(27) Cai, Y. C.; Shen, J.; Ge, G.; Zhang, Y. Z.; Jin, W. Q.; Huang, W.; Shao, J. J.; Yang, J.; Dong, X. C. Stretchable $Ti_3C_2T_x$ MXene/Carbon Nanotube Composite Based Strain Sensor with Ultrahigh Sensitivity and Tunable Sensing Range. *ACS Nano* **2018**, *12* (1), 56−62.
(28) Su, Y. S.; Yang, W. R.; Jheng, W. W.; Kuo, W.; Tzeng, S. D.; Yasuda, K.; Song, J. M. Optimization of Piezoresistive Strain Sensors Based on Gold Nanoparticle Deposits on PDMS Substrates for Highly Sensitive Human Pulse Sensing. *Nanomaterials* **2022**, *12* (13), No. 2312.
(29) Zheng, Y. J.; Li, Y. L.; Li, Z. Y.; Wang, Y. L.; Dai, K.; Zheng, G. Q.; Liu, C. T.; Shen, C. Y. The effect of filler dimensionality on the electromechanical performance of polydimethylsiloxane based conductive nanocomposites for flexible strain sensors. *Compos. Sci. Technol.* **2017**, *139*, 64−73.
(30) Kim, K.-H.; Jang, N.-S.; Ha, S.-H.; Cho, J. H.; Kim, J.-M. Highly Sensitive and Stretchable Resistive Strain Sensors Based on Microstructured Metal Nanowire/Elastomer Composite Films. *Small* **2018**, *14* (14), No. 1704232.
(31) Fu, R. F.; Warnakula, T.; Shi, Q. Q.; Yap, L. W.; Dong, D. S.; Liu, Y. Y.; Premaratne, M.; Cheng, W. L. Plasmene nanosheets as optical skin strain sensors. *Nanoscale Horiz.* **2020**, *5* (11), 1515−1523.
(32) Jeong, S.; Heo, S.; Kang, M.; Kim, H. J. Mechanical durability enhancement of gold-nanosheet stretchable electrodes for wearable human bio-signal detection. *Mater. Des.* **2020**, *196*, No. 109178.
(33) Li, X.; Zhang, R. J.; Yu, W. J.; Wang, K. L.; Wei, J. Q.; Wu, D. H.; Cao, A. Y.; Li, Z. H.; Cheng, Y.; Zheng, Q. S.; Ruoff, R. S.; Zhu, H. W. Stretchable and highly sensitive graphene-on-polymer strain sensors. *Sci. Rep.* **2012**, *2*, No. 870.
(34) Lim, G. H.; Lee, N. E.; Lim, B. Highly sensitive, tunable, and durable gold nanosheet strain sensors for human motion detection. *J. Mater. Chem. C* **2016**, *4* (24), 5642−5647.
(35) Naguib, M.; Kurtoglu, M.; Presser, V.; Lu, J.; Niu, J. J.; Heon, M.; Hultman, L.; Gogotsi, Y.; Barsoum, M. W. Two-Dimensional Nanocrystals Produced by Exfoliation of $Ti_3AlC_2$. *Adv. Mater.* **2011**, *23* (37), 4248−4253.
(36) Naguib, M.; Mochalin, V. N.; Barsoum, M. W.; Gogotsi, Y. 25th Anniversary Article: MXenes: A New Family of Two-Dimensional Materials. *Adv. Mater.* **2014**, *26* (7), 992−1005.
(37) Liu, A.; Qiu, H.; Lu, X. H.; Guo, H.; Hu, J. W.; Liang, C. B.; He, M. K.; Yu, Z.; Zhang, Y. L.; Kong, J.; Gu, J. W. Asymmetric Structural MXene/PBO Aerogels for High-Performance Electromagnetic Interference Shielding with Ultra-Low Reflection. *Adv. Mater.* **2025**, *37* (5), No. 2414085.
(38) Paramasivam, G.; Yadavali, S. P.; Atchudan, R.; Arya, S.; Sundramoorthy, A. K. Recent advances in the medical applications of two-dimensional MXene nanosheets. *Nanomedicine* **2024**, *19* (30), 2633−2654.
(39) Solangi, N. H.; Lingamdinne, L. P.; Karri, R. R.; Mubarak, N. M.; Mazari, S. A.; Koduru, J. R. Emerging 2D MXene quantum dots for catalytic conversion of $CO_2$. *Carbon* **2025**, *232*, No. 119758.
(40) Zeng, X. J.; Zhao, C.; Jiang, X.; Yu, R. H.; Che, R. C. Functional Tailoring of Multi-Dimensional Pure MXene Nanostructures for Significantly Accelerated Electromagnetic Wave Absorption. *Small* **2023**, *19* (41), No. 202303393.
(41) Zhou, Z. Y.; Pourhashem, S.; Wang, Z. Q.; Sun, J. W.; Ji, X. H.; Zhai, X. F.; Duan, J. Z.; Hou, B. R. Mxene structure: A key parameter in corrosion barrier performance of organic coatings. *J. Ind. Eng. Chem.* **2022**, *116*, 310−320.
(42) Yang, Y.; Shi, L.; Cao, Z.; Wang, R.; Sun, J. Strain Sensors with a High Sensitivity and a Wide Sensing Range Based on a $Ti_3C_2Ti_x$


https://doi.org/10.1021/acsanm.5c01438
*ACS Appl. Nano Mater.* 2025, 8, 10022−10032

(MXene) Nanoparticle-Nanosheet Hybrid Network. *Adv. Funct. Mater.* **2019**, *29* (14), No. 1807882.
(43) Cai, Y.; Shen, J.; Ge, G.; Zhang, Y.; Jin, W.; Huang, W.; Shao, J.; Yang, J.; Dong, X. Stretchable $Ti_3C_2T_x$ MXene/Carbon Nanotube Composite Based Strain Sensor with Ultrahigh Sensitivity and Tunable Sensing Range. *ACS Nano* **2018**, *12* (1), 56−62.



https://doi.org/10.1021/acsanm.5c01438
*ACS Appl. Nano Mater.* 2025, 8, 10022−10032